IET Nanobiotechnology

Special Issue: Selected extended papers from the 2nd International Conference on Nanoscience and Nanotechnology (ICNAN2019)

IET Journals
The Institution of Engineering and Technology

Synthesis of manganese doped β-FeOOH and $MnFe_2O_4$ nanorods for enhanced drug delivery and hyperthermia application

ISSN 1751-8741
Received on 17th March 2020
Revised 25th May 2020
Accepted on 10th July 2020
E-First on 2nd November 2020
doi: 10.1049/iet-nbt.2020.0098
www.ietdl.org

Chandunika R.K.[1], Vijayaraghavan Rajagopalan[2], Niroj Kumar Sahu[1] ✉

[1]*Centre for Nanotechnology Research, Vellore Institute of Technology, Vellore, TN 632014, India*
[2]*School of Advanced Sciences, Vellore Institute of Technology, Vellore, TN 632014, India*
✉ *E-mail: nirojs@vit.ac.in*

Abstract: Preparation of manganese ferrite ($MnFe_2O_4$) nanorods by the reduction of akaganeite seeds in the presence of oleylamine is reported. The Mn-doped β-FeOOH akaganeite seeds have been processed by the hydrolysis of metal-chloride salts in the presence of polyethylenimine (PEI) surfactant. The hydrophobic oleylamine capped nanorods are made hydrophilic using trisodium citrate as a phase transferring agent. The nanorods form with an aspect ratio of 5.47 and possess a high magnetisation value of 69 emu/g at an applied magnetic field of 1.5 T. The colloidal water dispersion of nanorods exhibits superior heating efficiency by the application of alternating magnetic field (AMF). A specific absorption rate value of 798 W/g is achieved at an applied AMF of field strength 500 Oe and frequency 316 kHz. Further, the citrate functionalised nanorods are capable of attaching with doxorubicin (DOX) electrostatically with a loading efficiency of 97% and the drug release is pH responsive. The DOX loaded nanorods show a promising effect on the apoptosis of MCF-7 as experimented in vitro.

1 Introduction

Cancer is the second globally leading fatal disease. In 2012, 14.1 million cancer cases were reported by the National Cancer Institute of America (NCI) [1] and increased to 18.1 million, with 9.6 million deaths in 2018 reported by the World Health Organization [2]. There are many associated side effects of conventional chemotherapy treatment of cancer and few cancer cells develop resistance to certain drugs. To overcome these issues, the current research is focused on the utilisation of nanotechnology in medicine. The unique physico-chemical properties of magnetic nanomaterials are extensively utilised in the field of drug delivery [3], hyperthermia [4, 5] and magnetic resonance imaging [6]. However, the application of magnetic nanoparticle (MNP) in cancer therapy is associated with many challenges and hence theranostics are still in the preclinical stage [7]. The biological application of MNP deals in the interface of physical, chemical and biological sciences. MNP generally possesses shape and size-dependent magnetic properties. Further, few of the MNP is non-toxic to human up to a certain concentration and are biocompatible [8, 9].

Different synthesis methods have been developed to fine control the morphology of MNPs [10–14]. In the biomedical field, most of the investigation has been carried on the spherical MNPs [6, 15]. However, the high aspect ratio of anisotropic 1D magnetic nanostructures, such as nanorods, nanowires and nanotubes, have drawn considerable attention due to their superior magnetic properties. The preparation of anisotropic iron nanorods by the reduction of β-FeOOH was first reported by Chen *et al.* [16]. Since then, extensive investigation on controlled morphology by the reduction of FeOOH was carried out by several researchers. Mohapatra *et al.* [17] reported that different lengths of β-FeOOH nanorods could be obtained by changing the ratio of polyethylenimine (PEI) in a hydrolysis method which further can be converted to Fe_3O_4 nanorods. Microwave-assisted methods have been adopted by Nikitin *et al.* [18] to synthesise Fe_3O_4 nanorods of the length of 20–30 nm by reducing β-FeOOH in the presence of hydrazine hydrate. It is also reported that 1D nanoparticles are advantageous in biomedical applications due to their high surface and long circulation time [19]. Kolhar *et al.* [20] reported that 1D nanomaterials had enhanced specific attachment to the targeted site compared to spherical structures. A study by Geng *et al.* [21] claims that anisotropic nanostructure possessed longer circulation time in blood compared to spherical particles. Some of the in vivo studies of nanorods also indicate lower toxicity [22, 23].

Keeping in mind the advantageous properties of nanorods for biological applications, we synthesise a novel Mn-doped β-FeOOH by the hydrolysis of chloride ions of $FeCl_3$ and $MnCl_2$ in the presence of PEI. Then, $MnFe_2O_4$ nanorods were prepared by the reduction method in the presence of oleylamine, which is schematically shown in Fig. 1. The physico-chemical properties of the nanorods were characterised and the potential of the nanorods in magnetic hyperthermia and drug delivery has been evaluated.

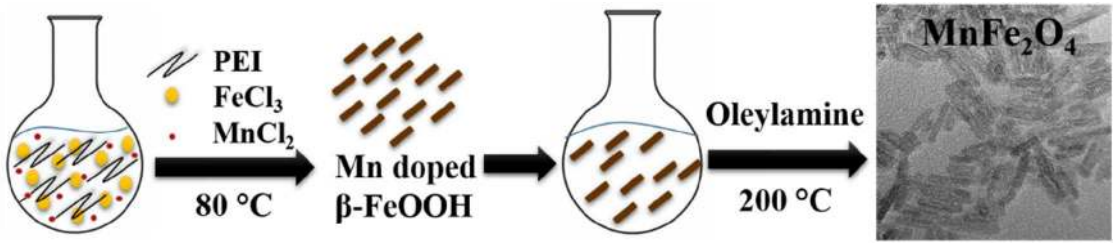

Fig. 1 *Schematic illustration of the synthesis of $MnFe_2O_4$ nanorods*

2 Experimental section

2.1 Materials used

All the chemicals were of analytical standard and used as received. Iron (III) chloride hexahydrate ($FeCl_3 \cdot 6H_2O$, 98.9% purity), manganese chloride (II) tetrahydrate ($MnCl_2 \cdot 4H_2O$, 98%), branched PEI solution (molecular weight 25 kDa), trisodium citrate (TSC), oleylamine (OLA) and ethanol were purchased from Sigma Aldrich, India. LA401 dialysis membrane-150 was purchased from Himedia. Milli-Q water was used for the experiment.

2.2 Preparation of Mn-doped β-FeOOH

A modified hydrolysis synthesis method was used to synthesise Mn-doped β-FeOOH nanorods (termed as Mn-β-FeOOH) with PEI, as reported elsewhere [17]. Briefly, 5 ml of PEI was dissolved in 100 ml of Milli-Q water in a 250 ml round bottom (RB) flask. Then, 5.4 g of $FeCl_3$ (0.2 mol) and 1.258 g of $MnCl_2$ (0.1 mol) were added in the PEI solution. The solution was heated at 80°C for 2 h in an oil bath under constant magnetic stirring. After 2 h, the mixture was allowed to cool to room temperature (RT) and the precipitates were isolated by centrifugation at 7000 rpm. The prepared Mn-β-FeOOH nanoparticles were collected, rinsed thoroughly with a mixture of water and ethanol and dried at 45°C.

2.3 Synthesis of $MnFe_2O_4$ nanorods

500 mg of Mn-β-FeOOH and 8 g of oleylamine (OLA) were mixed in a 100 ml RB flask. OLA plays a dual role of reducing agent and as a surfactant [24]. The mixture was magnetically stirred thoroughly under the nitrogen atmosphere. Then the reaction solution was heated to 100°C and maintained for 30 min to remove absorbed moisture and impurities from the solvent. Then, the temperature was raised to 200°C at a ramping rate of 5°C/min and retained for 4 h. A dark brownish precipitate was formed. Finally, the solution was allowed to cool to RT and precipitates were isolated by the magnetic separation method. The separation method was repeated for five times by adding 2 ml of hexane to disperse particles followed by the addition of ethanol as a flocculating agent. The OLA coated $MnFe_2O_4$ nanorods (OLA-$MnFe_2O_4$) was dispersed in hexane and stored.

2.4 Phase transfer by ligand exchange

To make the hydrophobic OLA coated $MnFe_2O_4$ nanorods hydrophilic, OLA has been replaced by citrate on the surface of nanorods via ligand exchange chemistry. In a typical procedure, the nanorods were precipitated from the hexane by adding excess ethanol and dried at 45°C. Then, 100 mg of nanorods added to the 100 ml of Milli-Q water containing 2.4 g of TSC. The solution was continuously stirred and maintained at 70°C for 2 h. Then, the surface-modified nanorods were isolated by centrifugation and washed thoroughly with a mixture of water and ethanol. Finally, the ligand exchanged TSC coated $MnFe_2O_4$ nanorods (TSC-$MnFe_2O_4$) were dispersed in Milli-Q water.

2.5 Sample characterisations

The XRD patterns of the samples were obtained by using an X-ray diffractometer (D8 Advance Bruker diffractometer), which utilises Cu-Kα radiation ($\lambda = 1.5405$ Å). Debye–Scherrer equation $d = k\lambda/(\beta\cos\theta)$ was used to calculate the crystallite size of the nanorods, where $\lambda = 1.5405$ Å, $k = 0.9$, θ = diffraction angle and β = full-width half-maximum. Microstructures of the nanorods are captured in a field emission gun transmission electron microscope (HR-TEM Tecnai G2, F30), which was operated at an accelerating potential of 300 kV. Magnetic measurements were recorded using vibrating sample magnetometer (VSM Lakeshore-7410). Fourier transform infrared (FTIR) spectra were recorded at the range of 400–4000 cm^{-1} in a Shimadzu IR Prestige instrument. The fluorescence measurements for drug release were carried out using the Hitachi F700 fluorescence spectrometer. X-ray photoelectron spectra (XPS) were recorded in the PHI Versaprobe III XPS instrument. Calorimetric magnetic hyperthermia experiments of the nanorods were performed using a 4.2-kW Ambrell EASYHEAT 8310.

3 Results and discussion

3.1 XRD, FTIR and thermogravimetric analysis (TGA)

The XRD patterns of Mn-β-FeOOH and OLA-$MnFe_2O_4$ nanorods are shown in Fig. 2*a*. The XRD patterns of Mn-β-FeOOH reveals the prominent peak positions at 2θ (degree) values of 12.17, 16.53, 26.91, 35.23, 39.34, 46.51, 52.47, 55.73, 61.95, and 64.66 corresponds to crystallographic planes (110), (200), (310), (211), (420), (411), (600), (521), (710), and (541), respectively, which are matched with the tetragonal phase of akaganeite (JCPDS card no 34-1266) [25]. The diffraction peaks found for OLA-$MnFe_2O_4$ at 2θ values of 30.22, 35.51, 43.20, 57.04, and 62.84 correspond to crystallographic planes (220), (311), (400), (422), (511), and (440), respectively. This suggests that $MnFe_2O_4$ forms in the spinel crystal structure (JCPDS card no 89-4319). Further, it reveals that Mn-β-FeOOH completely reduces to $MnFe_2O_4$. The crystallite sizes of Mn-β-FeOOH and OLA-$MnFe_2O_4$ are found to be 13 and 15 nm, respectively. To confirm the metallic state of the Mn and Fe, XPS analyses were carried out. The survey spectrum of Mn-β-FeOOH (supplementary Fig. S1) evidences the presence of $Mn2p_{1/2}$, $Mn2p_{3/2}$, $Fe2p_{1/2}$, $Fe2p_{3/2}$, O1s, and C1s. The O1s spectrum can be well deconvoluted into two peaks at 528.9 eV for metal-oxygen bond and 530.3 eV for the hydroxyl group in akaganeite. The Mn2p spectra can be deconvoluted into four sub-peaks of Mn^{3+} and Mn^{4+}, which proves the presence of Mn on akaganeite. The XPS of OLA-$MnFe_2O_4$ (supplementary Fig. S2) confirms the presence of Fe, Mn, O, and C. The C1s peak at 284.4 eV is originated from the organic OLA compounds on the surface of the nanoparticle. Two major peaks exhibited by Mn2p at binding energies of 641.31 and 653.06 eV correspond to $Mn2p_{1/2}$ and $Mn2p_{3/2}$, respectively, indicating the Mn^{2+} oxidation state. The energy difference of 11.75 eV is due to the spin-orbital splitting exhibited by Mn2p. No additional satellite peak is observed in Mn2p spectra implies the spinel phase formation of $MnFe_2O_4$. Fe2p spectra show two major components $Fe2p_{3/2}$ and $Fe2p_{1/2}$ at binding energies of 710.91 and 724.86 eV, respectively. This is due to the spin-orbital coupling between 3d electrons and 2p hole.

The FTIR spectra of Mn-β-FeOOH, OLA-$MnFe_2O_4$, and TSC-$MnFe_2O_4$ are shown in Fig. 2*b*. In akaganeite spectra, the vibrational band at 3242 cm^{-1} corresponds to the N–H bond in PEI. The band at 2970 cm^{-1} corresponds to the C–H stretching vibrations of an amine. The NH_2 wagging and scissoring of amine appear at 1460 and 1606 cm^{-1}, respectively. The bands at 437 and 655 cm^{-1} represent the metal oxide stretching bonds Fe–O and Mn–O [26]. In the FTIR spectra of OLA-$MnFe_2O_4$, the peaks at 2933 and 2839 cm^{-1} are assigned to vibrations from the CH_2 group of an amine. The vibrational bands at 1321 and 1631 cm^{-1} are attributed to the NH bending and NH_2 scissoring, respectively. The band at 1043 cm^{-1} assigned to the CH in-plane bending of oleylamine [27]. This proves the oleylamine coating on the surface of nanorods. Metal oxide (M-O) vibrational band is observed at 565 cm^{-1}. In the FTIR spectra of TSC-$MnFe_2O_4$, the broad peak at 3310 cm^{-1} is due to the O–H stretching. The C–H bending vibrations of sodium citrate are visible at 2987 and 2924 cm^{-1}. The sharp peak at 1618 cm^{-1} is appeared due to the C = O stretching [28]. These facts prove the successful ligand exchange and surface modification of nanorods by TSC.

The weight losses with temperature profiles have been investigated for nanorods by the TGA (Fig. 2*c*). TGA of Mn-β-FeOOH shows an initial weight loss of 9.6% up to 150°C as a result of the elimination of absorbed water molecules on the surface of the nanoparticles. The gradual weight loss up to 300°C and plateau occurs is due to the phase transition of akaganeite into $MnFe_2O_4$ [29]. The weight loss of OLA-$MnFe_2O_4$ occurs in three

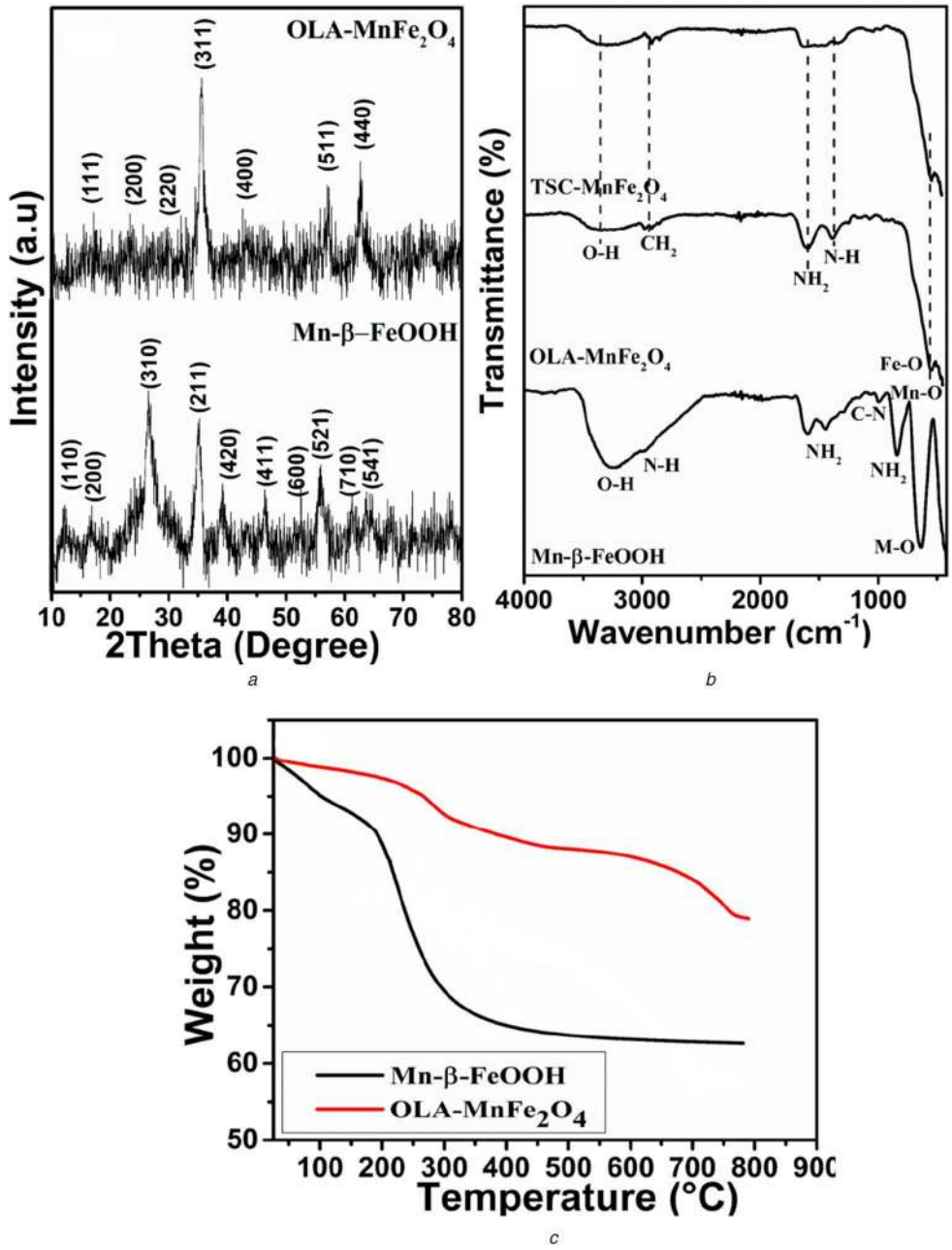

Fig. 2 *Material Properties*

(a) XRD pattern of Mn-β-FeOOH and OLA-$MnFe_2O_4$, ***(b)*** FTIR spectra of nanorods at different stages and, ***(c)*** Weight loss profile of the nanorods with temperature

stages. 2.8% of weight loss up to 150°C is due to the dehydration of adsorbed water molecules. Weight loss in the range of 150–450°C is due to the degradation of surface grafted oleylamine into a carbonaceous by-product. After 450°C, the weight loss is attributed to the oxidative phase transformation of ferrite phases. The TGA proves the formation of $MnFe_2O_4$ and surface grafted with oleylamine.

3.2 Microstructural analysis

The nanorod morphology of Mn-β-FeOOH and OLA-$MnFe_2O_4$ is clearly seen in the TEM images (Fig. 3). The Mn-doped akaganeite have a length of 15 ± 0.8 nm and a width of 2 ± 0.6 nm, whereas OLA-$MnFe_2O_4$ nanorods have a length of 16 ± 0.7 nm and a width of 3 ± 0.2 nm. OLA-$MnFe_2O_4$ nanorods form with an average aspect ratio of 5.47. It is observed that when akaganeite reduced to form $MnFe_2O_4$ nanorods, the dimension is slightly increased; however, the morphology remains intact.

3.3 Magnetic properties analysis

The magnetisation of OLA-$MnFe_2O_4$ nanorods with respect to the applied magnetic field (*M–H* curve) is shown in Fig. 4. The nanorods exhibit ferromagnetic behaviour with a saturation magnetisation (*Ms*) value of 69.3 emu/g and coercivity (*Hc*) of 116 Oe. The nanorods possess substantially higher *Ms* value as compared to the few earlier reported value [30, 31]. Mohapatra *et al.* [17] reported *Ms* value of 50 emu/g for Fe_3O_4 nanorods of a length of 30 nm, whereas Nikitin *et al*. [18] reported *Ms* value of 54.4 emu/g for Fe_3O_4 nanorods of a length 21 nm. The *Ms* value of bulk $MnFe_2O_4$ is 80 emu/g [32]. The reduction in *Ms* value of the nanorods as compared to the bulk value may be due to (i) weak exchange coupling between bulk atoms as there are a large fraction of surface atoms in the nanoparticles, (ii) the spin canting effect of the surface atoms, and (iii) the presence of surfactant oleylamine molecules which is diamagnetic in nature. Theoretically, all the Fe ions are trivalent (Fe^{3+}) and Mn ions are divalent (Mn^{2+}) in spinel $MnFe_2O_4$ with a magnetic moment of 5 μ_B per formula unit according to Néel model. However, it is evident from XPS that there is the presence of Mn^{3+} in the nanorods, which might be

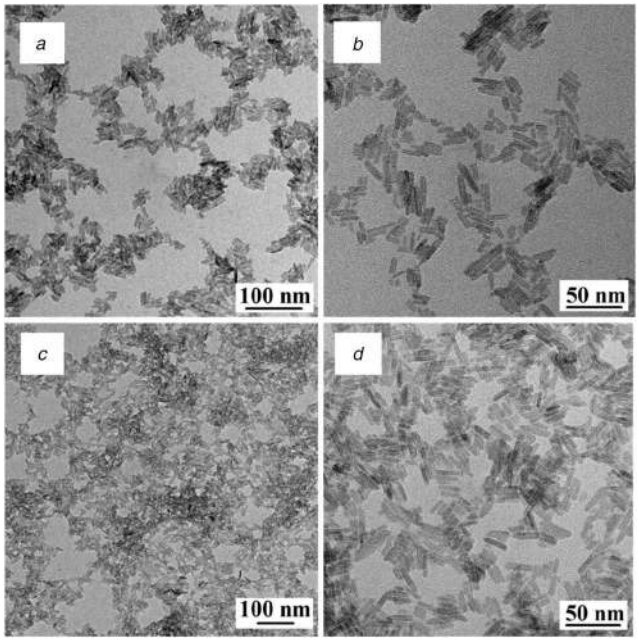

Fig. 3 *HRTEM images of*
(a), ***(b)*** Mn-β-FeOOH and, ***(c)***, ***(d)*** OLA-$MnFe_2O_4$ at different magnifications

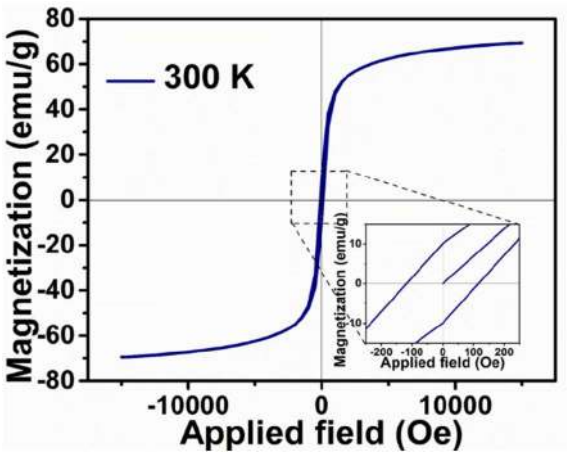

Fig. 4 *M-H curve of OLA-$MnFe_2O_4$ measure in RT*

counterbalanced by Fe^{2+} ions or some vacancies, which leads to canted spins. Such observation is reported by Sawatzky *et al.* [33] in spinel ferrites via Mössbauer spectra. The initial slope of the *M–H* curve is very steep may be due to the finite size and surface effect of the nanorods. This explains the particles are single domain in nature with negligible coercivity and remanent magnetisation suitable for biomedical applications [34–37]. In general, elongated particles are highly sensitive towards the applied magnetic field than the particles with lower aspect ratio and the coercivity increases with the decrease of aspect ratio [38]. This is another major reason for the use of nanorods in magnetic field-based applications such as hyperthermia.

3.4 DOX loading and release studies

A DOX stock solution was prepared by dissolving 5 mg of DOX in 10 ml of Milli-Q water at a concentration of 0.5 mg/ml and stored at 4°C in the deep freezer for use. To obtain the DOX calibration graph, the peak area obtained from fluorescence data for each concentration is plotted against the respective concentration.

The DOX loading studies were carried with TSC-$MnFe_2O_4$. All the experiments were conducted in a dark environment for preventing photodegradation of DOX. 10 mg of nanorods was incubated with 50 µl of DOX solution in a vial and the total volume was made up to 3 ml by adding Milli-Q water. The nanorod-DOX solution was kept in a shaker for 24 h at RT. The cationic drug DOX getting loaded on the nanorods by electrostatic attraction of the O^- group of trisodium citrate and daunosamine group of DOX as schematically shown in Fig. 5*a*. After incubation, the nanorods were isolated by the magnetic separation method and the fluorescence spectra of supernatant were measured at an excitation wavelength of 480 nm and emission in the range of 500–650 nm. The loading efficiency was calculated comparing with the standard curve and the loading efficiency was found to be around 97%. The high loading efficiency can be attributed to the high surface area of the rod-shaped nanoparticles, effective surface functionalisation of the nanorods with TSC through ligand exchange and efficient electrostatic attachment.

The release profile of drug from DOX loaded TSC-$MnFe_2O_4$ was investigated in the physiological pH of 7.4 and acidic pH of 5.5 to mimic the physiological environment of normal cells and the endosomal environment of cancer cells, respectively. The DOX loaded nanorods were dispersed separately in 1 ml of phosphate buffer solution (PBS) of pH 7.4 and acidic PBS (diluted with HCl) of pH 5.5 and transferred into two separate membranes. The sample loaded membranes were kept immersed in 20 ml of PBS buffer solution with a steady stirring of 150 rpm. At different time intervals, the 3 ml of PBS solution was collected from the 20 ml bath for drug release analysis and fresh 3 ml PBS buffer was added subsequently into the solution. The percentage of cumulative release was calculated from the intensity of the fluorescence spectrum. The drug release profiles up to 60 h of release in two

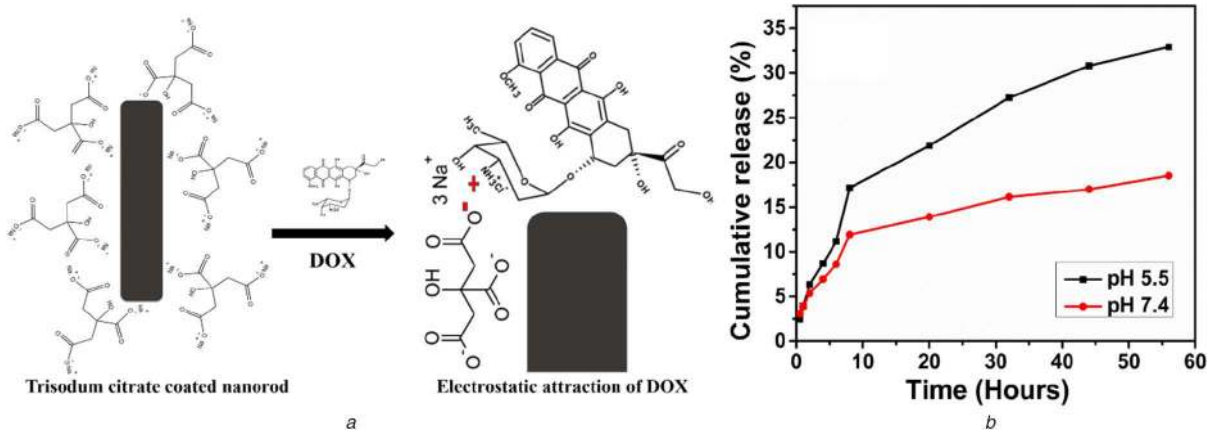

Fig. 5 *Drug loading and release behaviours*

(a) Schematic representation of the electrostatic drug loading mechanism on TSC-$MnFe_2O_4$ and, ***(b)*** Release profile of DOX from the nanorods at different pH conditions

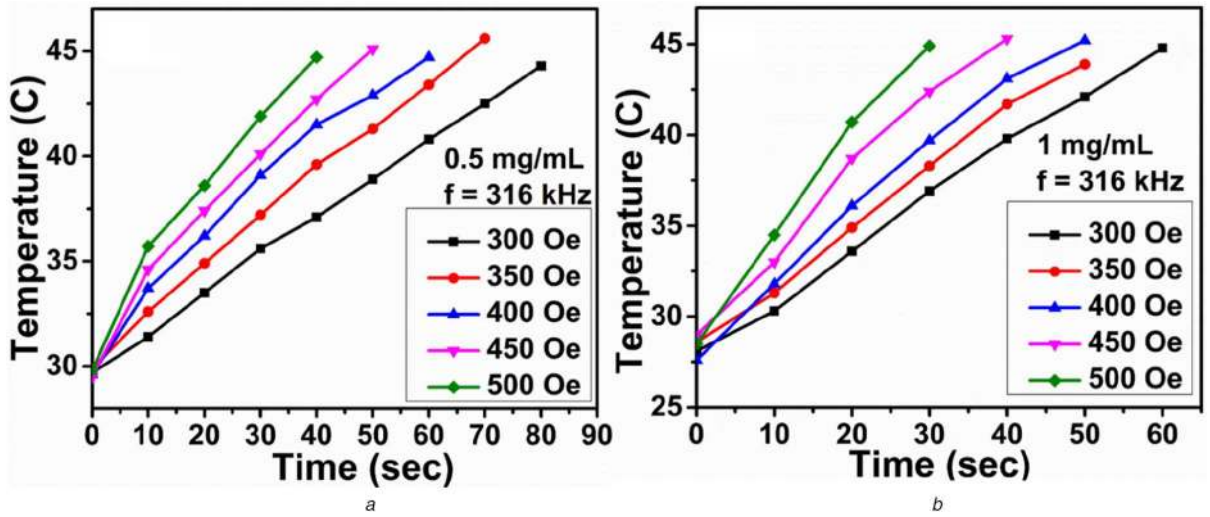

Fig. 6 *Inductive heating profile of TSC-$MnFe_2O_4$ colloidal suspension at different concentrations of*

(a) 0.5 mg/ml and, ***(b)*** 1 mg/ml. The measurements were done with the application of AMF of different field strength and frequency

different pH conditions are shown in Fig. 5*b*. Sustained drug release patterns are observed in both pH environments; however, the release rate is higher in the acidic environment. This suggests the drug release is pH stimulated, which may be beneficial for drug release at intercellular compartments of cancerous cells. Two-stage drug release patterns are observed. In the first 10 h, a burst release like a profile of drug with 11.93 and 17.16% release are seen at pH 7.4 and pH 5.5, respectively, which may be due to the surface absorbed drug molecules [39]. According to the Higuchi model, this drug release may be diffusion-controlled irrespective of the different pH [40]. In acidic pH, the negative ions present in the trisodium citrate tend to accept more H^+ ion, which might weaken the electrostatic attraction and hence more DOX release [41]. Such pH sensitive release has been reported in different drug delivery systems [42, 43].

3.5 Magnetic hyperthermia study

The magnetic hyperthermia efficiency depends on the material properties such as morphology, size, colloidal stability and magnetic properties. When MNPs are exposed to an alternating magnetic field (AMF), the heat dissipation occurs via hysteresis loss and loss due to magnetic moment relaxation. Multiple domain particles dissipate heat through hysteresis losses, whereas particles in a single domain and superparamagnetic regime dissipate heat by Néel and Brownian relaxations. When superparamagnetic particles are exposed to AMF, the heat is dissipated by the rotation of moments of the particles referred to as Néel relaxation, whereas the physical rotation of particles with a change in the field within a medium is referred as Brownian relaxation [44].

The heat generated from MNP colloids is quantified by specific absorption rate (SAR) which is calculated using the following formula:

$$\mathrm{SAR} = C_{\mathrm{water}} \times \frac{1}{m} \times \frac{\Delta T}{\Delta t} \tag{1}$$

where C_{water} is the specific heat of water, which is equal to 4.2 J $g^{-1}{}^{\circ}C^{-1}$, m is the mass of the nanoparticles in aqueous suspension and $\Delta T/\Delta t$ is the initial slope of the temperature–time curve.

The heating profiles of nanorods at two different concentrations of 1 and 0.5 mg/ml under applied AMF of field strength 300, 350, 400, 450, and 500 Oe and fixed frequency of 316 Hz are shown in Fig. 6. The increase in the hyperthermia temperature of 42–45°C was attained by both concentrations. The heat generation is found to be both concentrations as well applied field strength dependent. Hyperthermia temperature is attained faster in the suspension of a higher concentration than the lower concentration at the application of the same field strength. The calculated SAR values are tabulated in Table 1. The highest SAR values of 798 W/g were obtained for the concentration of 1 mg/ml at an applied field of 500 Oe. The observed SAR values due to the increased shape anisotropy are comparatively higher compared with few earlier reports on the ferrite nanorods [18, 45–48], which are tabulated in supplementary information (Table S1). Moreover, the SAR values in nanorods are superior to reported spherical shape nanoparticles. These results inferred that shape anisotropy of the particle influence the magnetic hyperthermia heating performance.

Table 1 SAR values of nanorods for two concentrations at different ac applied field

Applied field, Oe	SAR values, W/g	
	1 mg/ml	0.5 mg/ml
300	415	302
350	466	387
400	552	423
450	630	506
500	798	618

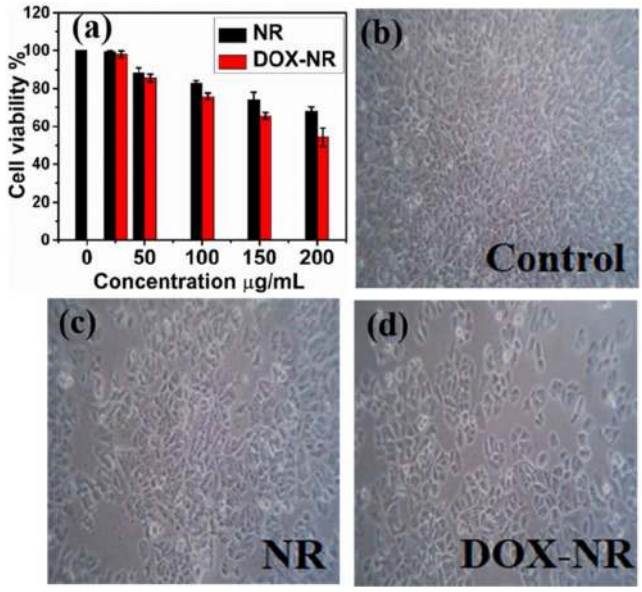

Fig. 7 *Cytotoxicity of MCF-7 cells*
(a) Histogram plot, ***(b)*** Optical image of control cells, ***(c)*** Optical image of cells after treated with nanorods (NR) at conc. of 200 μg/ml and, ***(d)*** Optical image of cells after treated with DOX loaded nanorods (DOX-NR) at conc. of 200 μg/ml

3.6 In-vitro cytotoxicity study

Standard MTT assay was performed for cytotoxicity evaluation of bare and DOX loaded nanorods in human breast cancer (MCF-7) cells. 1×10^4 cells/well were grown in 96 well plates supplemented with DMEM media, containing 10% foetal bovine serum and 1X antibiotic antimycotic solution. The cells were incubated in a CO_2 incubator at 37°C. The cells were aspirated with PBS twice and treated with 200 μl of DMEM solution containing nanorods of different concentrations and incubated for 24 h. After incubation, the medium was washed from cells. Then, 50 μl MTT solution (concentration of 0.5 mg/ml of PBS) was added and incubated for another 4 h. After 4 h of incubation, the MTT containing medium from the cells was removed and washed using 200 μl of PBS. The absorbance was measured by a microplate reader at 570 nm by the development of colour intensity from formazan dye and the cell viability % (average of triplicate data) was calculated using the following equation:

$$\text{Cell viability } \% = \frac{P_{\text{absorbance}}}{C_{\text{absorbance}}} \times 100 \quad (2)$$

where $C_{\text{absorbance}}$ is the absorbance of only cell line and $P_{\text{absorbance}}$ is the absorbance from the particle loaded well.

The MCF-7 cell viability against TSC-$MnFe_2O_4$ nanorods (NRs) and DOX loaded nanorods (DOX-NRs) at different concentrations of 25, 50, 100, 150, and 200 μg/ml is shown in Fig. 7. Both bare and drug-loaded particles show significant cell death with an increase in concentration. The exact % cell viability triplicate values and microscopic images of MCF-7 cell with and without drug-loaded nanorods at different concentrations of the nanomaterial are given in supplementary Figs. S3, S4 and Tables S2, S3. The nanorods impose oxidative stress on the cell wall. Further, there may be leaching out of the metal ions such as Fe^{3+}, Fe^{2+}, and Mn^{2+} in the acidic intercellular environment, which is well known for the generation reactive oxygen species and as a result there is cell apoptosis [49]. The apoptosis is amplified while treating with DOX loaded nanorods may be due to combining the effect of enhanced DOX release from the nanoparticles in acidic pH and release of metal ions. Also, the pKa value of trisodium citrate is ∼3.05 and hence in the acid environment of cancer cells, the electrostatic interaction between TSC and DOX gets weak, leading to more release of DOX and promotes more apoptosis. The overall cell death percentage at the material concentration of 200 μg/ml with and without DOX is found to be ∼46 and 32%, respectively, which suggests that there is controlled apoptosis when treated with $MnFe_2O_4$ nanorods as a therapeutic carrier. The optical images of MCF-7 incubated with NR (in supplementary Fig. S3) do not show many changes, whereas optical images (in supplementary Fig. S4) of DOX-NR incubated MCF-7 cells show significant changes in the morphology of cells and clear spherical patches are visible corresponds to cell apoptosis.

4 Conclusion

Monodispersed $MnFe_2O_4$ nanorods with an aspect ratio of 5.47 form when Mn-doped β-FeOOH thermally decomposed in the presence of oleylamine as a reducing agent. The hydrophobic nanorods can be made hydrophilic by replacing OLA with TSC through the ligand exchange mechanism. The citrate functionalised nanorods are attached to the DOX molecule efficiently via electrostatic interaction. There is sustained and pH responsive release of DOX from the DOX loaded nanorods. $MnFe_2O_4$ nanorods possess superior magnetic properties and colloidal stability and show efficient inductive heating capability. The SAR values are found to be dependent on the concentration of the nanoparticles in the dispersion as well on the field strength of AMF. Furthermore, this method of preparation of monodispersed $MnFe_2O_4$ nanorods is very simple and shows promising results towards hyperthermia and in-vitro cytotoxicity of the MCF-7 cancer cell.

5 Acknowledgment

The authors gratefully acknowledge the financial support from DST-SERB, Government of India (project grant no. ECR/2016/000301).

6 References

[1] Torre, L.A., Bray, F., Siegel, R.L., *et al.*: 'Global cancer statistics, 2012', *CA-Cancer J. Clin.*, 2015, **65**, (2), pp. 87–108
[2] 'World Health Organization, Cancer Fact Sheet, World Health Organization, Geneva, Switzerland', 2018
[3] Sahu, N.K., Gupta, J., Bahadur, D.: 'Pegylated FePt–Fe_3O_4 composite nanoassemblies (cnas): in vitro hyperthermia, drug delivery and generation of reactive oxygen species (ros)', *Dalton Trans.*, 2015, **44**, (19), pp. 9103–9113
[4] Cherukuri, P., Glazer, E.S., Curley, S.A.: 'Targeted hyperthermia using metal nanoparticles', *Adv. Drug Deliv. Rev.*, 2010, **62**, (3), pp. 339–345
[5] Tseng, H.-Y., Lee, G.-B., Lee, C.-Y., *et al.*: 'Localised heating of tumours utilising injectable magnetic nanoparticles for hyperthermia cancer therapy', *IET Nanobiotechnol.*, 2009, **3**, (2), pp. 46–54
[6] Kumar, S., Daverey, A., Khalilzad-Sharghi, V., *et al.*: 'Theranostic fluorescent silica encapsulated magnetic nanoassemblies for in vitro mri imaging and hyperthermia', *RSC Adv.*, 2015, **5**, (66), pp. 53180–53188
[7] Riegler, J., Wells, J.A., Kyrtatos, P.G., *et al.*: 'Targeted magnetic delivery and tracking of cells using a magnetic resonance imaging system', *Biomaterials*, 2010, **31**, (20), pp. 5366–5371
[8] Maier-Hauff, K., Ulrich, F., Nestler, D., *et al.*: 'Efficacy and safety of intratumoral thermotherapy using magnetic iron-oxide nanoparticles combined with external beam radiotherapy on patients with recurrent glioblastoma multiforme', *J. Neurooncol.*, 2011, **103**, (2), pp. 317–324
[9] Lu, M., Cohen, M.H., Rieves, D., *et al.*: 'Fda report: ferumoxytol for intravenous iron therapy in adult patients with chronic kidney disease', *Am. J. Hematol.*, 2010, **85**, (5), pp. 315–319
[10] Daou, T.J., Pourroy, G., Bégin-Colin, S., *et al.*: 'Hydrothermal synthesis of monodisperse magnetite nanoparticles', *Chem. Mater.*, 2006, **18**, (18), pp. 4399–4404
[11] Li, W., Lee, S.S., Wu, J., *et al.*: 'Shape and size controlled synthesis of uniform iron oxide nanocrystals through new non-hydrolytic routes', *Nanotechnology*, 2016, **27**, (32), p. 324002

[12] Ramachandra Kurup Sasikala, A., Thomas, R.G., Unnithan, A.R., *et al.*: 'Multifunctional nanocarpets for cancer theranostics: remotely controlled graphene nanoheaters for thermo-chemosensitisation and magnetic resonance imaging', *Sci. Rep.*, 2016, **6**, (1), p. 20543

[13] Chandunika, R.K., Rajagopalan, V., Niroj Kumar, S.: 'Magnetic hyperthermia application of $MnFe_2O_4$ nanostructures processed through solvents with the varying boiling point', *Mater. Res. Express*, 2020, **7**, (6), p. 064002, https://doi.org/10.1088/2053-1591/ab955e

[14] Rajan, S.A., Sharma, M., Sahu, N.K.: 'Water-to-peg variation: morphology and hyperthermic behaviour of iron oxide', *J. Supercond. Novel Magn.*, 2020, **33**, (9), pp. 1603–1609

[15] Abenojar, E.C., Wickramasinghe, S., Bas-Concepcion, J., *et al.*: 'Structural effects on the magnetic hyperthermia properties of iron oxide nanoparticles', *Prog. Nat. Sci.: Mater. Int.*, 2016, **26**, (5), pp. 440–448

[16] Min, C., Bo, T., Nikles, D.E.: 'Preparation of iron nanoparticles by reduction of acicular/spl beta/-FeOOH particles', *IEEE Trans. Magn.*, 1998, **34**, (4), pp. 1141–1143

[17] Mohapatra, J., Mitra, A., Tyagi, H., *et al.*: 'Iron oxide nanorods as high-performance magnetic resonance imaging contrast agents', *Nanoscale*, 2015, **7**, (20), pp. 9174–9184

[18] Nikitin, A., Khramtsov, M., Garanina, A., *et al.*: 'Synthesis of iron oxide nanorods for enhanced magnetic hyperthermia', *J. Magn. Magn. Mater.*, 2019, **469**, pp. 443–449

[19] Li, F., Xu, H., Sun, P., *et al.*: 'Size effects of magnetic beads in circulating tumour cells magnetic capture based on streptavidin–biotin complexation', *IET Nanobiotechnol.*, 2019, **13**, (1), pp. 6–11

[20] Kolhar, P., Anselmo, A.C., Gupta, V., *et al.*: 'Using shape effects to target antibody-coated nanoparticles to lung and brain endothelium', *Proc. Natl. Acad. Sci.*, 2013, **110**, (26), pp. 10753–10758

[21] Geng, Y., Dalhaimer, P., Cai, S., *et al.*: 'Shape effects of filaments versus spherical particles in flow and drug delivery', *Nat. Nanotechnol.*, 2007, **2**, (4), pp. 249–255

[22] Alkilany, A.M., Thompson, L.B., Boulos, S.P., *et al.*: 'Gold nanorods: their potential for photothermal therapeutics and drug delivery, tempered by the complexity of their biological interactions', *Adv. Drug Deliv. Rev.*, 2012, **64**, (2), pp. 190–199

[23] Huang, X., Li, L., Liu, T., *et al.*: 'The shape effect of mesoporous silica nanoparticles on biodistribution, clearance, and biocompatibility in vivo', *ACS Nano*, 2011, **5**, (7), pp. 5390–5399

[24] Mourdikoudis, S., Liz-Marzán, L.M.: 'Oleylamine in nanoparticle synthesis', *Chem. Mater.*, 2013, **25**, (9), pp. 1465–1476

[25] Jung, J., Song, K., Bae, D.R., *et al.*: 'B-FeOOH nanorod bundles with highly enhanced round-trip efficiency and extremely low overpotential for lithium air batteries', *Nanoscale*, 2013, **5**, (23), pp. 11845–11849

[26] Murad, E., Bishop, J.L.: 'The infrared Spectrum of synthetic akaganéite, B-FeOOH', *Am. Mineral.*, 2000, **85**, (5), pp. 716–721

[27] Chen, M., Feng, Y.-G., Wang, X., *et al.*: 'Silver nanoparticles capped by oleylamine: formation, growth, and self-organization', *Langmuir*, 2007, **23**, (10), pp. 5296–5304

[28] Thottoli, A.K., Unni, A.K.A.: 'Effect of trisodium citrate concentration on the particle growth of ZnS nanoparticles', *J. Nanostruct. Chem.*, 2013, **3**, (1), p. 56

[29] Fan, J., Zhao, Z., Ding, Z., *et al.*: 'Synthesis of different crystallographic FeOOH catalysts for peroxymonosulfate activation towards organic matter degradation', *RSC Adv.*, 2018, **8**, (13), pp. 7269–7279

[30] Wang, J., Chen, Q., Hou, B., *et al.*: 'Synthesis and magnetic properties of single-crystals of $MnFe_2O_4$ nanorods', *Eur. J. Inorg. Chem.*, 2004, **2004**, (6), pp. 1165–1168

[31] Leung, K., Wáng, Y.-X.: 'Mn-Fe nanowires towards cell labeling and magnetic resonance imaging' in Lupu, N. (Ed.): *Nanowires science and technology* (Intech, Croatia, 2010), pp. 331–344

[32] Vamvakidis, K., Katsikini, M., Sakellari, D., *et al.*: 'Reducing the inversion degree of Mnfe2o4 nanoparticles through synthesis to enhance magnetization: evaluation of their 1 (H) NMR relaxation and heating efficiency', *Dalton Trans.*, 2014, **43**, (33), pp. 12754–12765

[33] Sawatzky, G.A., Van Der Woude, F., Morrish, A.H.: 'Ossbauer study of several ferrimagnetic spinels', *Phys. Rev.*, 1969, **187**, (2), pp. 747–757

[34] Salehnia, Z., Shahbazi-Gahrouei, D., Akbarzadeh, A., *et al.*: 'Synthesis and characterisation of iron oxide nanoparticles conjugated with epidermal growth factor receptor (egfr) monoclonal antibody as mri contrast agent for cancer detection', *IET Nanobiotechnol.*, 2019, **13**, (4), pp. 400–406

[35] Marins, J.A., Montagnon, T., Ezzaier, H., *et al.*: 'Colloidal stability of aqueous suspensions of polymer-coated iron oxide nanorods: implications for biomedical applications', *ACS Appl. Nano Mater.*, 2018, **1**, (12), pp. 6760–6772

[36] Li, C., Feng, K., Xie, N., *et al.*: 'Mesoporous silica-coated gold nanorods with designable anchor peptides for chemo-photothermal cancer therapy', *ACS Appl. Nano Mater.*, 2020, **3**, (6), pp. 5070–5078

[37] Sánchez-Cabezas, S., Montes-Robles, R., Gallo, J., *et al.*: 'Combining magnetic hyperthermia and dual T1/T2 Mr imaging using highly versatile iron oxide nanoparticles', *Dalton Trans.*, 2019, **48**, (12), pp. 3883–3892

[38] He, X., Zhong, W., Au, C.T., *et al.*: 'Size dependence of the magnetic properties of Ni nanoparticles prepared by thermal decomposition method', *Nanoscale Res. Lett.*, 2013, **8**, (1), p. 446

[39] Mi, Y., Liu, X., Zhao, J., *et al.*: 'Multimodality treatment of cancer with herceptin conjugated, thermomagnetic iron oxides and docetaxel loaded nanoparticles of biodegradable polymers', *Biomaterials*, 2012, **33**, (30), pp. 7519–7529

[40] Barick, K.C., Singh, S., Jadhav, N.V., *et al.*: 'pH-responsive peptide mimic shell cross-linked magnetic nanocarriers for combination therapy', *Adv. Funct. Mater.*, 2012, **22**, (23), pp. 4975–4984

[41] Curry, D., Cameron, A., MacDonald, B., *et al.*: 'Adsorption of doxorubicin on citrate-capped gold nanoparticles: insights into engineering potent chemotherapeutic delivery systems', *Nanoscale*, 2015, **7**, (46), pp. 19611–19619

[42] Sahu, N.K., Gupta, J., Bahadur, D.: 'Pegylated fept-Fe3o4 composite nanoassemblies (CNAS): in vitro hyperthermia, drug delivery and generation of reactive oxygen Species (ROS)', *Dalton Trans.*, 2015, **44**, (19), pp. 9103–9113

[43] Zhang, F., Braun, G.B., Pallaoro, A., *et al.*: 'Mesoporous multifunctional upconversion luminescent and magnetic 'nanorattle' materials for targeted chemotherapy', *Nano Lett.*, 2012, **12**, (1), pp. 61–67

[44] Suriyanto. Ng, E.Y., Kumar, S.D.: 'Physical mechanism and modeling of heat generation and transfer in magnetic fluid hyperthermia through Neelian and Brownian relaxation: a review', *Biomed. Eng. Online*, 2017, **16**, (1), p. 36

[45] Simeonidis, K., Morales, M.P., Marciello, M., *et al.*: 'In-situ particles reorientation during magnetic hyperthermia application: shape matters twice', *Sci. Rep.*, 2016, **6**, (1), p. 38382

[46] Das, R., Alonso, J., Nemati Porshokouh, Z., *et al.*: 'Tunable high aspect ratio iron oxide nanorods for enhanced hyperthermia', *J. Phys. Chem. C*, 2016, **120**, (18), pp. 10086–10093

[47] Geng, S., Yang, H., Ren, X., *et al.*: 'Anisotropic magnetite nanorods for enhanced magnetic hyperthermia', *Chem. Asian J.*, 2016, **11**, (21), pp. 2996–3000

[48] Reyes-Ortega, F., Checa Fernandez, B.L., Delgado, A.V., *et al.*: 'Hyperthermia-triggered doxorubicin release from polymer-coated magnetic nanorods', *Pharmaceutics.*, 2019, **11**, (10), pp. 517–520

[49] Rangam, N., Jaiswal, A., Bellare, J., *et al.*: 'Synthesis of surface grafted mesoporous magnetic nanoparticles for cancer therapy', *J. Nanosci. Nanotechnol.*, 2017, **17**, (8), pp. 5181–5188